


Photoemission spectrum of Ca_2RuO_4 : Spin polaron physics in an $S = 1$ antiferromagnet with anisotropies

Adam Kłosiński ^{1,*}, Dmitri V. Efremov,² Jeroen van den Brink,^{2,3} and Krzysztof Wohlfeld ¹

¹*Institute of Theoretical Physics, Faculty of Physics, University of Warsaw, Pasteura 5, PL-02093 Warsaw, Poland*

²*IFW Dresden, Helmholtzstraße 20, 01069 Dresden, Germany*

³*Department of Physics, Technical University Dresden, Helmholtzstraße 10, 01069 Dresden, Germany*

 (Received 11 October 2019; revised manuscript received 20 December 2019; published 13 January 2020)

We derive an $S = 1$ spin polaron model which describes the motion of a single hole introduced into the $S = 1$ spin antiferromagnetic ground state of Ca_2RuO_4 . We solve the model using the self-consistent Born approximation and show that its hole spectral function qualitatively agrees with the experimentally observed high-binding energy part of the Ca_2RuO_4 photoemission spectrum. We explain the observed peculiarities of the photoemission spectrum by linking them to two anisotropies present in the employed model: The spin anisotropy and the hopping anisotropy. We verify that these anisotropies, and *not* the possible differences between the ruthenate ($S = 1$) and the cuprate ($S = \frac{1}{2}$) spin polaron models, are responsible for the strong qualitative differences between the photoemission spectrum of Ca_2RuO_4 and of the undoped cuprates.

DOI: [10.1103/PhysRevB.101.035115](https://doi.org/10.1103/PhysRevB.101.035115)

I. INTRODUCTION

Understanding the strongly correlated physics of transition metal oxides constitutes a nontrivial task [1–5]. One reason is that the simplest, but still realistic, effective models for the electronic structure of these materials normally contain degrees of freedom of different type, such as charge, spin, lattice, and orbital ones. Even the most boiled-down versions of such interacting models are rarely solvable in the thermodynamic limit. In practice, the sweet spot is hit by theoretical models that can be solved without severe approximations *and* at the same time can explain certain salient experimental features of a correlated oxide. One such case, already known since the end of the 1980's, involves the so-called spin polaron problem in which a propagating charge couples to magnetic degrees of freedom [6–13]. Spin polaron physics explains dispersive features observed in the photoemission spectrum of the (spin $S = \frac{1}{2}$) antiferromagnetically ordered and Mott insulating copper oxides [14–18]. It turns out that the electronic dispersion found in the spectra of the insulating parent compounds of the high-temperature superconductors can be well explained using a t - J or Hubbard model that is mapped onto a (spin) polaron problem.

It is remarkable that despite the still unresolved mystery of high-temperature superconductivity in doped copper oxides, undoped cuprates are by far the simplest class of materials to model as far as correlated oxides go. This is because the very starting point, the uncorrelated model Hamiltonian, is well described by a single, partially filled band [3,19], a situation only most rarely encountered in the manganites, vanadates, nickelates, or, in fact, the ruthenates that we investigate here [2,5]. In almost all oxides the effective models are more involved and go far beyond the single-band t - J or Hubbard

variety that is relevant for the cuprates. The question arises as to how spin polaron physics fares in such a more complex situation.

In this context we take a close look at the intensively investigated ruthenium oxide Ca_2RuO_4 [20–36] which is the Mott insulating analog of the unconventional superconductor Sr_2RuO_4 [37]. At low temperature the insulating state is an ordered spin $S = 1$ antiferromagnet [22,26,28,32,35]. Recently, the detailed photoemission spectrum of this Mott insulator was not only studied experimentally, but also successfully modeled using a multiband Hubbard Hamiltonian [30]. But, since this theoretical approach relies on treating the multiband Hubbard model within single-site dynamical mean-field theory, it is not clear in what shape or form spin polaron physics remains relevant.

Here we specifically investigate the origin of the incoherent and almost momentum-independent part of the Ca_2RuO_4 photoemission spectrum: Its high-binding energy part [see the yellow rectangle of Fig. 1(a)] associated with a single-hole motion in the xz and yz orbitals [30]. The reason for leaving the xy orbital out of our analysis is that the highly dispersive, quasiparticlelike part of the photoemission spectrum stretching from low- to high-binding energy [see Fig. 1(a)] can be easily understood as free hole motion within the xy orbitals. This conclusion follows from the observation that the relatively large energy gap between the xy and xz/yz orbitals leads to the xy orbital being fully occupied while at the same time mixing between xy and xz/yz orbitals is absent from either the nearest-neighbor hopping or the Coulomb part of the Hamiltonian. This being understood, there is not much to be gained by including the xy orbitals in our analysis and thus from here on we concentrate on the physics emerging from the xz/yz ones.

To summarize, our aim is altogether twofold: We wish to understand the high-binding energy part of the photoemission spectrum of Ca_2RuO_4 from a realistic $S = 1$ *spin polaron*

*adam.klosinski@fuw.edu.pl

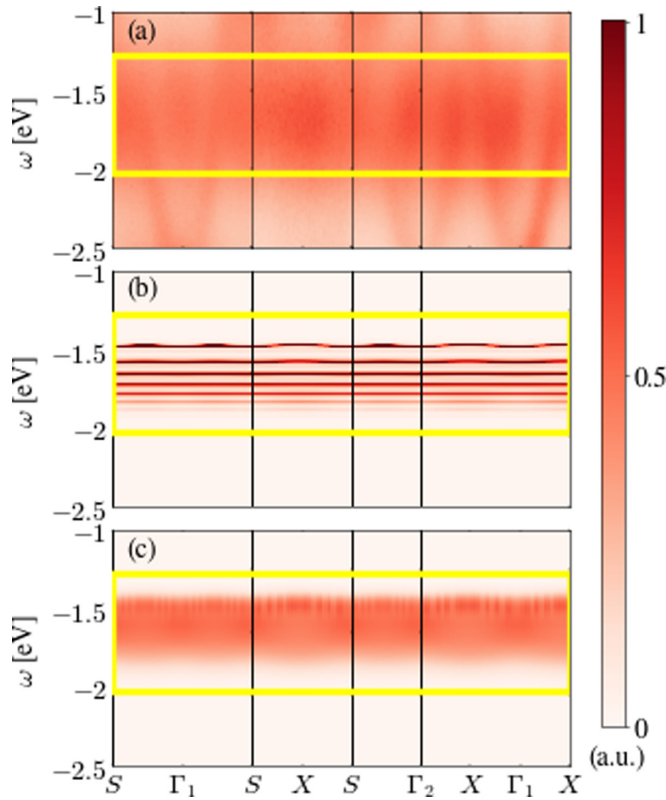


FIG. 1. Comparison between the experimental and theoretical spectral functions of Ca_2RuO_4 : (a) angle-resolved photoemission (ARPES) spectrum of Ca_2RuO_4 as published in Ref. [30]; (b) hole spectral function $A(\mathbf{k}, \omega)$ calculated for the spin $S = 1$ t - J Hamiltonian (1) and (2) with $\mathbf{e}_{xz} = \hat{x}$, $\mathbf{e}_{yz} = \hat{y}$ and using the mapping onto the spin polaron Hamiltonian (6) and the SCBA method (see text) with model (6) parameters: $t = 22J$, $\epsilon = 5.6J$, $\gamma = 0.25J$, $J = 5.6$ meV, numerical broadening of $A(\mathbf{k}, \omega)$ $\delta = 0.22J$; (c) hole spectral function $A(\mathbf{k}, \omega)$ calculated as in (b) but convoluted with a Gaussian with the half-width at half-maximum equal to $0.5t$, in accordance with the approximate experimental resolution of the ARPES measurements [30]. The yellow rectangles mark the high-binding energy parts of the spectra that are incoherent and almost momentum independent. They are identified in ARPES as having a dominant xz/yz orbital character [30], and are theoretically modeled by (b). [The dispersive branch visible in (a), both inside and outside of the yellow rectangle and not discussed here, is associated with the xy orbital [30]. See main text of the paper.] Theoretical spectra (b) and (c) are normalized in the same manner as the ARPES spectrum (a) of Ref. [30].

model for this material which then is to offer insight into the more general question as to which extent such an $S = 1$ spin polaron problem is different from the “standard” (i.e., $S = \frac{1}{2}$) spin polaron physics known from the cuprates.

The paper is organized as follows. In Sec. II we introduce the t - J model that describes the motion of a single hole in the ground state of Ca_2RuO_4 . Next, in Sec. III we map the t - J model onto a $S = 1$ spin polaron model. The latter is solved using the self-consistent Born approximation (SCBA) in Sec. IV. Finally, we discuss the obtained results in Sec. V and end the paper with conclusions in Sec. VI. The paper is supplemented by an Appendix which contains details on the mapping of the t - J to the polaron model.

II. t - J MODEL

In order to model (the high-binding energy part of) the photoemission spectrum of Ca_2RuO_4 , we follow the well-developed scheme mentioned in the Introduction, which was successfully used to describe, *inter alia*, the photoemission spectra of several undoped copper oxides [14–18]. Thus, we consider an appropriate t - J -like Hamiltonian constructed as a sum of two parts $\mathcal{H} = \mathcal{H}_J + \mathcal{H}_t$.

The first part, \mathcal{H}_J , describes the low-energy physics of Mott insulating Ca_2RuO_4 in terms of the interaction between the localized $S = 1$ magnetic moments. The relevant magnetic Hamiltonian is well known in this case and reads as [26,28,29],

$$\mathcal{H}_J = J \sum_{\langle i,j \rangle} \mathbf{S}_i \cdot \mathbf{S}_j + \epsilon \sum_i (S_i^z)^2 + \gamma \sum_i (S_i^x)^2, \quad (1)$$

where the summation runs over all nearest-neighbor pairs on a two-dimensional (2D) square lattice, J is the spin exchange constant, and \mathbf{S}_i are the spin $S = 1$ operators. As already discussed in Refs. [26,28,29] the spin model is highly anisotropic, with the suggested values of the \hat{z} (\hat{x}) axis anisotropy being equal to $\epsilon = 5.6J$ ($\gamma = 0.25J$), respectively, with $J = 5.6$ meV reproducing the spin wave dispersion observed in the inelastic neutron scattering experiment [26,28,29]. We note that such a large spin anisotropy originates from the substantial spin-orbit coupling of ruthenium which is, however, not strong enough to stabilize the $S = 0$ ground state [22,26,28,32,35]. Although the latter result can naively be understood as a consequence of the crystal-field splitting (between the xz , yz , and the xy orbitals) being about twice larger than the spin-orbit coupling [32] and therefore the spin $S = 0$ states having considerably higher energy than the spin $S = 1$ states (see Fig. S1 of [29]), it has been postulated [29,36,38,39] that nevertheless the “excitonic magnetism” can be at play here. In particular, in Ref. [40] the authors suggest the latter scenario for Ca_2RuO_4 although they also advocate that a pronounced orbital polarization is present in the system.

The second part of the Hamiltonian, \mathcal{H}_t , is the kinetic term. It describes the motion of charge carriers within the ruthenium oxide plane, for instance, the motion of a single hole created by the photoemission process. As discussed above, we restrict our model to the xz and yz orbitals and end up with

$$\mathcal{H}_t = -t \sum_{i,\sigma} (\tilde{c}_{i+\mathbf{e}_{xz},\sigma}^\dagger \tilde{c}_{i,xz,\sigma} + \tilde{c}_{i+\mathbf{e}_{yz},\sigma}^\dagger \tilde{c}_{i,yz,\sigma} + \text{H.c.}), \quad (2)$$

where the first (second) term describes the hoppings of an electron with spin σ between the nearest-neighbor ruthenium xz (yz) orbitals along the $\mathbf{e}_{xz} = \hat{x}$ ($\mathbf{e}_{yz} = \hat{y}$) direction in the 2D square lattice, respectively. The effectively one-dimensional (“directional”) hoppings follow from the Slater-Koster scheme [41] applied to the square-lattice geometry of the ruthenium oxide plane [24] and is a common feature of systems with active $\{xz, yz\}$ orbital degrees of freedom [42]. For the value of the hopping element t in Ca_2RuO_4 we take $t = 123$ meV [25], i.e., $t = 22J$ when $J = 5.6$ meV. To simplify the analysis, we do not take into account the spin-orbit coupling between holes in the xz and yz orbitals. This simplification is not *a priori* justified for a realistic situation in Ca_2RuO_4 but is rationalized by the intuitive understanding

of its spectral functions presented in Ref. [30], which relies on the Hund's coupling and does not include the spin-orbit coupling as an essential part. Moreover, the (surprisingly) good agreement between the theoretical results presented below and the experimental results (cf. Fig. 1) legitimizes this assumption *a posteriori*. Possible intrinsic differences between the $S = \frac{1}{2}$ and $S = 1$ spin polaron models which we wish to identify should also be considered irrespective of the spin-orbit coupling.

Two projections are used in the kinetic Hamiltonian (2). First, due to the strong onsite Coulomb repulsion U , and since we confine ourselves to the low-energy physics valid for energies smaller than the Hubbard U , we restrict the hole motion to the Hilbert space spanned by the local ruthenium d^2 and d^1 multiplets. [Note that since the xy orbital is considered to be "always" occupied by two electrons in the studied model [22,25,30], the xy electrons are integrated out and effectively the nominal occupancy of the ruthenium ions is not d^4 (d^3) but d^2 (d^1) in the undoped (single-hole) case, respectively.] As typical to any t - J -like model [43], we use the tildes above the electron creation and annihilation operators to formally denote this constraint. Second, just as in the case of the ground state (see discussion above), we project out the local spin singlet $S = 0$ states. Altogether, the t - J Hamiltonian is rather complex, for it contains the $S = 1$ operators in the spin part as well as the two projection operators in the kinetic part. Therefore, in Appendix A we rewrite the above model using the convenient representation of the Hubbard operators [44] (for a more recent application, see also [45,46]), which allows one to express the projections explicitly.

Having discussed the t - J Hamiltonian for the doped Ca_2RuO_4 in detail, let us stress that the above model can be regarded to a large extent as a proper *microscopic* model for the doped ruthenate. In particular, this concerns the t part of the model, which basically follows from the tight-binding description of the LDA bands (see above and Ref. [25]). We note that Ca_2RuO_4 is not a charge-transfer but a Mott-Hubbard insulator [21,47] and therefore the Zhang-Rice singlet construction [19] is not needed, for both the doped holes as well as electrons go to the ruthenium d orbitals. On the other hand, the situation with the J part is a bit more subtle. In principle, the spin model for Ca_2RuO_4 was originally proposed by Kunkemoeller *et al.* [28] on the phenomenological grounds, for its form was postulated by comparing the calculated spin wave spectrum to the observed inelastic neutron scattering spectrum. However, a similar model was discussed also in Ref. [29] and in the Supplemental Material of that reference it was suggested that such a phenomenological model may be obtained from a realistic electronic structure of Ca_2RuO_4 (in the limit of strong correlations and relatively large spin-orbit coupling with respect to the crystal-field splitting).

Finally, as we are interested in the photoemission spectrum, we define the following orbitally resolved hole spectral function:

$$A_\alpha(\mathbf{k}, \omega) = -\frac{1}{\pi} \text{Im} \langle 0 | \tilde{c}_{\mathbf{k},\alpha,\sigma}^\dagger \frac{1}{\omega - \mathcal{H} + E_0 + i\delta} \tilde{c}_{\mathbf{k},\alpha,\sigma} | 0 \rangle, \quad (3)$$

where $|0\rangle$ is the ground state of the undoped t - J model (1), (2) with energy E_0 , δ is the infinitesimally small broadening that is nevertheless finite in the numerical calculations below, and

we explicitly keep the orbital index $\alpha \in \{xz, yz\}$ but suppress the spin index σ (the spectral function is spin independent). In what follows, we are also interested in the orbitally integrated spectral function which is defined in the usual way as $A(\mathbf{k}, \omega) = \sum_\alpha A_\alpha(\mathbf{k}, \omega)$.

III. FROM t - J TO POLARON MODEL

Stimulated by the successful description of the photoemission spectra of the undoped cuprates [8,10,11,14–18] and to gain a better insight into the physics of the photoemission problem, we perform a mapping of the $S = 1$ t - J problem onto an $S = 1$ spin polaron problem. This is done in two steps.

First, we introduce the slave fermions

$$\tilde{c}_{i,\alpha,\uparrow} \rightarrow \hat{A} h_{i,\alpha}^\dagger, \quad (4)$$

$$\tilde{c}_{i,\alpha,\downarrow} \rightarrow \hat{A} h_{i,\alpha}^\dagger S_i^+ / \sqrt{2}, \quad (5)$$

where $h_{i,\alpha}^\dagger$ is the creation operator for a spinless hole on site i and orbital α , S_i^+ is the spin $S = 1$ operator on site i , and \hat{A} is an operator yet to be determined. The factor $1/\sqrt{2}$ in Eq. (5) normalizes the spin operator. It can be shown that in the Hilbert space being considered, the \hat{A} operator is diagonal and an explicit expression for it can be found. On the left-hand side of the mapping [Eqs. (4) and (5)], there is an implicit projection on the $S = 1$ spin triplet, which introduces factors of $1/\sqrt{2}$ each time the annihilation operator acts on the $S_z = 0$ states. This leads to the eigenvalue of \hat{A} equal to $\sqrt{2}$ for the $S_z = 0$ states and equal to 1 otherwise. Second, we rotate spins on one of the antiferromagnetic sublattices and express the spin operators through bosonic operators by way of the Holstein-Primakoff transformation. Finally, we use the linear spin wave approximation and the Bogoliubov transformation to diagonalize the resulting spin Hamiltonian (see Appendix B for details).

In the end we are left with a diagonal magnon term and a vertex coupling spinless holes to magnons in the following $S = 1$ spin polaron Hamiltonian:

$$\begin{aligned} H = H_t + H_J \approx & \sum_{\mathbf{q}} \Omega_{\mathbf{q}} \beta_{\mathbf{q}}^\dagger \beta_{\mathbf{q}} + E_0 \\ & + \frac{\sqrt{2}t}{\sqrt{N}} \sum_{\mathbf{k}, \mathbf{q}} [(\gamma_{k_x} v_{\mathbf{q}} + \gamma_{k_x - q_x} u_{\mathbf{q}}) h_{\mathbf{k},xz}^\dagger h_{\mathbf{k}-\mathbf{q},xz} \beta_{\mathbf{q}} \\ & + (\gamma_{k_y} v_{\mathbf{q}} + \gamma_{k_y - q_y} u_{\mathbf{q}}) h_{\mathbf{k},yz}^\dagger h_{\mathbf{k}-\mathbf{q},yz} \beta_{\mathbf{q}} + \text{H.c.}], \quad (6) \end{aligned}$$

where $\gamma_{k_i} = \cos(k_i)$ and $\beta_{\mathbf{q}}$ are the Bogoliubov boson (magnon) annihilation operators. $u_{\mathbf{q}}, v_{\mathbf{q}}$ are the Bogoliubov coefficients (see Appendix B for details). The above transformations also lead directly to the expression for the spectral function in terms of the spinless hole Green's function (see Appendix B for details):

$$A_\alpha(\mathbf{k}, \omega) = -\frac{1}{\pi} \text{Im} \langle 0 | h_{\mathbf{k},\alpha} \frac{1}{\omega - H + E_0 + i\delta} h_{\mathbf{k},\alpha}^\dagger | 0 \rangle. \quad (7)$$

IV. METHODS AND RESULTS

We calculate the hole spectral function $A_\alpha(\mathbf{k}, \omega)$ using the self-consistent Born approximation (SCBA) (see Ref. [7]).

Such approach has been successful in obtaining the cuprate spectral functions [7–11,13] and amounts to neglecting the so-called crossing diagrams and summing all the other (“rainbow diagrams”) to infinite order. The resulting self-consistent expressions for the self-energies and the Green’s function are given in Appendix B. These equations are then solved numerically on a finite lattice of 36×36 \mathbf{k} points. The resulting orbitally integrated hole spectral function $A(\mathbf{k}, \omega)$ is calculated for the realistic parameters of the model (see above) and is shown in Fig. 1(b).

The calculated hole spectral function qualitatively reproduces the incoherent and almost momentum-independent spectrum observed in the high-binding energy part of Ca_2RuO_4 photoemission results found in Ref. [30] and reproduced in Fig. 1(a). Although the onset of several horizontal “stripes” in the theoretical spectrum (see below) make the similarities between the theoretical and experimental spectral functions less apparent at first sight [Fig. 1(b)], a convolution of the theoretical spectral function with the available experimental resolution of ca. $0.5t$ yields a spectrum [Fig. 1(c)] which surprisingly well resembles the high-binding energy part of the observed experimental spectrum [Fig. 1(a)]: Both spectra have an incoherent character, without a clear quasi-particle band emerging, and only very weak dependence of its intensity on the momentum. (A weak dependence on the momentum of the intensities in the high-binding energy part of the observed experimental spectrum [Fig. 1(a)] originates in the xy orbital spectral function, not considered here but explained in detail in Ref. [30].) What is more, the low- and high-energy edges of both broad spectra are basically momentum independent. Finally, also the overall energy scale, which is given by the width of the broad spectrum estimated at the half-maximum intensity, is of the same order of magnitude in both cases and amounts to about 0.5 eV.

V. DISCUSSION

A. Spectral functions

The first question that arises concerns the origin of the onset of the incoherent, almost momentum-independent and, apart from the horizontal stripes, rather featureless spectrum of Fig. 1(b). Looking first at models (1) and (2) we can immediately note what distinguishes it from the “standard” $S = \frac{1}{2}$ t - J model, that has been widely used to describe the photoemission spectra of the undoped cuprates [6–11] and for which such a broad and flat incoherent band has not been observed. The most apparent are the two anisotropies. The spin anisotropy reflects the distortion of the lattice and leads to the γ and ϵ terms in Eq. (1). The perfect hopping anisotropy, on the other hand, which has its origin in the nominal valence of the ruthenium ions and the geometry of the ruthenium-oxide plane, leads to an effectively one-dimensional hole motion [cf. Eq. (2)]. On top of that, a more subtle distinction is related to the larger value of the spin $S = 1$ in the studied model. The latter leads to the onset of additional projection operators in the hopping part of the Hamiltonian. We explore the above-listed differences in detail by comparing the spectral function $A(\mathbf{k}, \omega)$ calculated for the distinct versions of the relevant t - J models (cf. Fig. 2). We see that (i) both hopping and

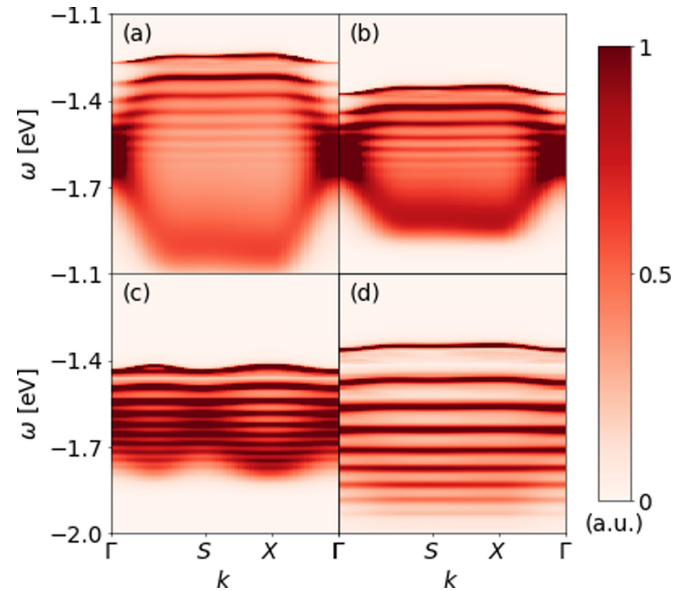


FIG. 2. The hole spectral functions $A(\mathbf{k}, \omega)$ obtained for distinct versions of the relevant t - J models and calculated by mapping onto the spin polaronic model and using the SCBA method (see text): (a) the standard spin $S = \frac{1}{2}$ t - J model but with twice larger magnon energy (cf. Ref. [7]); (b) spin $S = 1$ t - J model with neither the spin nor the hopping anisotropy, i.e., models (1) and (2) with $\epsilon = \gamma \equiv 0$ and $\mathbf{e}_{xz} \equiv \mathbf{e}_{yz} \in \{\hat{x}, \hat{y}\}$; (c) the spin $S = 1$ t - J model with the hopping anisotropy as suggested for Ca_2RuO_4 but no spin anisotropy, i.e., models (1) and (2) with $\mathbf{e}_{xz} = \hat{x}$, $\mathbf{e}_{yz} = \hat{y}$, and $\epsilon = \gamma \equiv 0$; (d) the spin $S = 1$ t - J model with only the spin anisotropy, i.e., (1) and (2) with $\epsilon, \gamma \neq 0$ and $\mathbf{e}_{xz} \equiv \mathbf{e}_{yz} \in \{\hat{x}, \hat{y}\}$. All spectra normalized as in Fig. 1.

spin anisotropies qualitatively change the spectrum of the $S = 1$ t - J model; (ii) the hopping anisotropy [see Fig. 2(c)] leads to the formation of a ladderlike spectrum with a relatively well-visible, momentum-dependent, incoherent part; (iii) the spin anisotropy [see Fig. 2(d)] leads to the onset of a well-visible ladderlike spectrum. Moreover, including both anisotropies in the calculations leads to the spectrum already presented in Fig. 1(b), which is qualitatively the same as the spectrum of the $S = 1$ t - J model with only the spin anisotropy [see Fig. 2(d)]. This shows that, for realistic values of model parameters, the spin anisotropy plays a dominant role in shaping the $A(k, \omega)$ spectral function. Albeit, if one were looking at the orbitally resolved spectral function, the impact of the hopping anisotropy would be more pronounced (see discussion of Fig. 3).

The formation of the ladderlike spectrum in the case of the spin anisotropy can be understood when one considers the fact that the very large anisotropy limit leads, in this case, to the dominant Ising-type interactions between spins. This triggers the hole confinement in a linear string potential and leads to a well-known ladderlike spectrum with the horizontal stripes [1,7,13]. On the other hand, for the hopping anisotropy, the emergence of a partially ladderlike spectrum is a consequence of the fact that the spin waves are still two dimensional, but the hopping is already one dimensional. This amplifies the coupling between holes and magnons, leading to an effectively smaller ratio of J/t in Fig. 2 case (c) vs case (b) and the stronger tendency toward the ladderlike spectrum

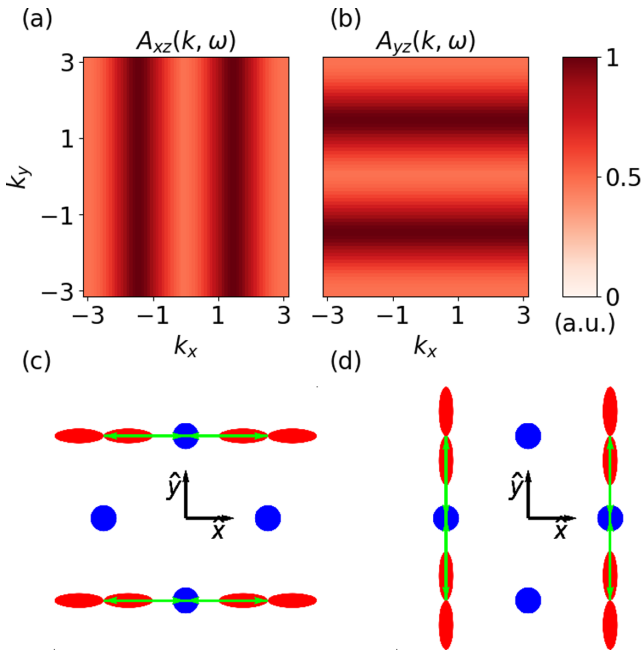


FIG. 3. The one-dimensional character of the orbitally resolved hole spectral function: (a) constant-energy cut of the spectral function $A_{xz}(\mathbf{k}, \omega_c)$ for a hole introduced into the xz orbital ($\omega_c = -2.1$ eV); (b) constant-energy cut of the spectral function $A_{yz}(\mathbf{k}, \omega_c)$ for a hole introduced into the yz orbital ($\omega_c = -2.1$ eV); (c), (d) a schematic view of the ruthenium-oxygen plane explaining the dominant one-dimensional character of the electronic hopping processes on the single-particle level that is also inherited by the many-body hopping processes of Eq. (2). For the xz (yz) orbital, only hopping in the \hat{x} (\hat{y}) direction is possible (cf. panel (c) [(d)] [41,42]). The oxygen (ruthenium) orbitals are shown in blue (red).

[7]. In order to better illustrate the one-dimensional character of the spectral function in Figs. 1 and 2(c), in Fig. 3 we present the constant energy cuts of two spectral functions, one describing a hole in the xz orbital, the other a hole in the yz orbital. We see that the one-dimensional hole motion, a consequence of the geometry of the ruthenium-oxygen plane and the vanishing of the transfer integrals between the oxygen p orbitals and some of the t_{2g} orbitals [42], is reflected in the hole spectral functions. They both show a manifestly one-dimensional dispersion, very much unlike what we see, for instance, in the copper oxides [14–18]. We note that, while including a finite spin-orbit coupling for holes in the xz or yz orbitals would naturally lead to the “mixing” between the one-dimensional bands, a good agreement between the theoretical and experimental spectra suggests that such an effect should be small in Ca_2RuO_4 .

Finally, with all other parameters equal, the fact that we do not consider here a spin $S = \frac{1}{2}$ (which would be formed by a single hole or electron per site) but a spin $S = 1$ antiferromagnet (two holes on each site) does not influence the spectral function qualitatively, thus, the difference between these two cases is purely quantitative [cf. Figs. 2(a) and 2(b)]. To understand why it is so, let us compare the possible hole-hopping processes in the $S = \frac{1}{2}$ and $S = 1$ antiferromagnet, which are represented schematically in Fig. 4. What we can conclude by looking at the process represented on the bottom

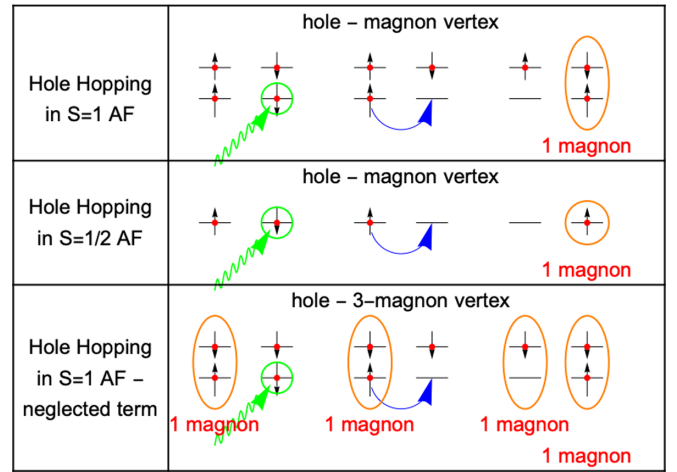


FIG. 4. A schematic view of the possible nearest-neighbor hole hoppings in the $S = 1$ and $S = \frac{1}{2}$ antiferromagnet (AF). (Top panel) A hopping process in the $S = 1$ antiferromagnet that, according to the here studied t - J Hamiltonian (1), (2), leads to the creation of one magnon in the effective $S = 1$ spin polaron model (6). (Middle panel) An analogous hopping process as above but in the $S = \frac{1}{2}$ antiferromagnet which, according to the standard t - J Hamiltonian [43], leads to the creation of one magnon in the spin polaron model of Ref. [7]. (Bottom panel) A hopping process in the $S = 1$ antiferromagnet that, according to the here studied t - J Hamiltonian (1), (2), leads to the creation of three magnons and is *neglected* in the $S = 1$ spin polaron model (6) for it goes beyond the linear spin wave approximation.

panel is that all the more complex processes, which have no analog in the single hole per site case, involve more than one magnon. In fact, they involve either three or five magnons, which is why we exclude them in the spin wave approximation employed here and why they are absent from Hamiltonian (6). Consequently, only the simplest process remains, the one analogous to the only process possible in the spin $S = \frac{1}{2}$ case (cf. the first two panels of Fig. 4). We stress that such a similarity between the hole moving in the $S = \frac{1}{2}$ and the $S = 1$ antiferromagnet would not be achieved in the classical double-exchange picture [48], for the latter one would not allow for the existence of the $|1, 0\rangle$ states on any site.

B. Spin polaron ground state

In order to shed more light on the ground states of all the t - J models considered so far, we carried out an analysis of the spin polaron as it appears in each of the models, following Ref. [8]. In Fig. 5 we show the contributions (spectral weights) A_k^n of the first four n -magnon wave functions to the full ground-state wave function in the SCBA approximation, the so-called Reiter’s wave function [49]. For the sake of numerical convergence, which could not be obtained for the small value of $J \lesssim 0.05t$, all the results were calculated for the “canonical value” of $J = 0.4t$. Thus, Fig. 5 only serves the purpose of comparing all the relevant models and does not give the quantitatively correct values for Ca_2RuO_4 .

We observe that, as we include the additional anisotropies, the overlap between the ground state and the 0-magnon

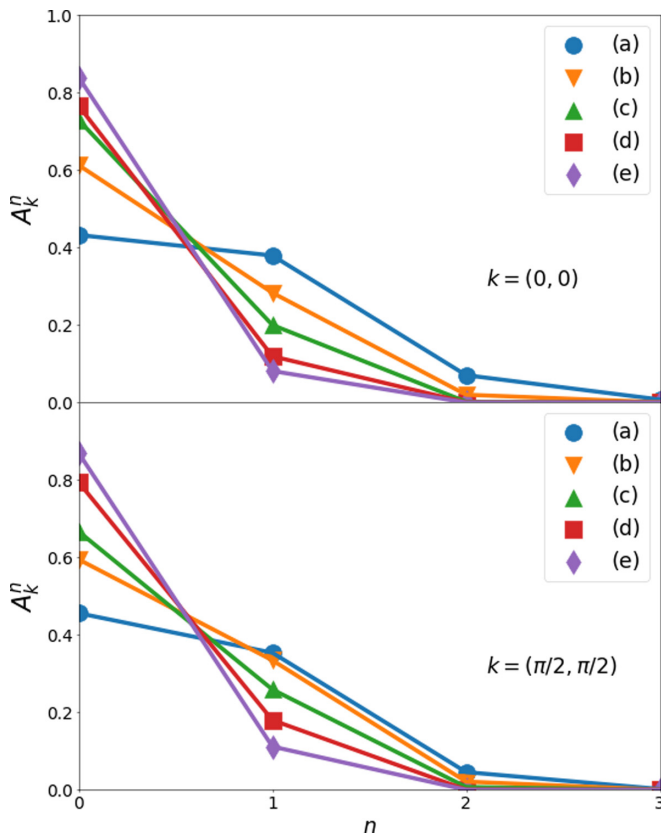


FIG. 5. The n -magnon contributions to the ground-state wave function in the SCBA approximation A_k^n (probabilities that the ground-state wave function at momentum \mathbf{k} contains n magnons). Each line represents a different t - J model: (a) the standard $S = \frac{1}{2}$ model but with twice larger magnon energy [cf. Fig. 2(a)]; (b) the $S = 1$ model with neither the spin nor the hopping anisotropy [cf. Fig. 2(b)]; (c) the $S = 1$ model with the hopping anisotropy but no spin anisotropy [cf. Fig. 2(c)]; (d) the $S = 1$ model with only the spin anisotropy [cf. Fig. 2(d)]; (e) the $S = 1$ model as proposed for Ca_2RuO_4 , i.e., with both the hopping and spin anisotropy [cf. Fig. 1(b)]. All results obtained for $J = 0.4 t$ and all other parameters as in Figs. 1 and 2.

wave function increases, while the 1-, 2- and 3-magnon contributions decrease. The increasing spectral weight of the 0-magnon term in the ground-state wave function, and therefore the increasing quasiparticle spectral weight, has two origins. *First*, looking at the $S = \frac{1}{2}$ and $S = 1$ t - J models, we note that the quasiparticle gains weight as we move from the former to the latter model. Interestingly, the twofold increase in the value of magnon energy as one goes from the $S = \frac{1}{2}$ to $S = 1$ does not explain this behavior since we have doubled the magnon energy in the $S = \frac{1}{2}$ t - J model to compensate for this phenomenon. Instead, this difference in quasiparticle weights is a result of the lower hole hopping energy in the $S = 1$ with respect to the $S = \frac{1}{2}$ t - J model: In the former the vertex acquires an additional factor of $1/\sqrt{2}$ due to the projection onto the $S = 1$ triplet. This is a consequence of Hund's coupling (see Appendix B for details) and is also visible in Fig. 2 [compare (a) vs (b)] as an overall narrowing of the spectral function. *Second*, the quasiparticle weight increases as we introduce the hopping and spin anisotropies.

In case of the hopping anisotropy, this is also a consequence of the lower hopping energy: For the 1D hopping the hole kinetic energy is twice smaller than in the 2D case. Finally, in the case of the spin anisotropy, the increased quasiparticle weight can be understood using an analogy to the t - J_z model since the anisotropy parameters ϵ and γ both introduce a magnon gap and make the magnon dispersion flatter. This makes it more costly for the terms with magnons to appear in the ground-state wave function, thus decreasing the probabilities A_k^n for $n \neq 0$. In the t - J_z model the magnon energy is always finite and independent on the lattice momentum and, consequently, the quasiparticle has more weight [8].

Regarding a more realistic value of J , one expects that the lower the magnon energy, the greater the average number of magnons $\langle n_k \rangle = \sum_n n A_k^n$ in the spin polaron ground state. Indeed, for the standard $S = \frac{1}{2}$ t - J model, Ramšak and Horsch [8] have shown that as J decreases the quasiparticle weight decreases and the maximum of A_k^n shifts toward higher values of n . Thus, for a realistic value of $J \simeq 0.045t$ in Ca_2RuO_4 we expect the quasiparticle weight to be much smaller than the ones shown in Fig. 5 and the A_k^n , $n \neq 0$, to be respectively larger. However, the general trend of decreasing $\langle n_k \rangle$ as one goes from $S = \frac{1}{2}$ to $S = 1$ and introduces the spin and hopping anisotropies will prevail. Finally, the spin polaron will, by “adiabatic continuity,” always have a nonzero quasiparticle component as long as $J \neq 0$ for all the discussed models in this subsection. Thus, we can conclude that the ground-state wave function of the model describing Ca_2RuO_4 can indeed be regarded as a “genuine” spin polaron and that its quasiparticle weight should be large with respect to the value of the spin exchange J , mostly due to the spin and hopping anisotropies.

VI. CONCLUSIONS

We have shown how a relatively simple spin $S = 1$ t - J model, that was mapped onto an $S = 1$ spin polaron model, can qualitatively reproduce the high-binding energy part of the observed Ca_2RuO_4 photoemission spectrum. In particular, we were able to explain the observed incoherent and almost momentum-independent photoemission spectrum by linking these peculiar features of the spectrum to two anisotropies present in the employed spin polaron model: The spin anisotropy [28] and the hopping anisotropy [30,42].

Interestingly, the differences between the spectral functions of the standard spin polaron model well known from the cuprates (i.e., spin $S = \frac{1}{2}$) and the model for Ca_2RuO_4 should not be regarded as being intrinsic to the $S = 1$ spin polaron model: They are all related to the above-mentioned strong anisotropies present in the model suggested for Ca_2RuO_4 and *not* to the potential differences between the hole moving in the $S = \frac{1}{2}$ and the $S = 1$ antiferromagnets. These turn out to be basically irrelevant in the linear spin wave approximation. Such a result can naturally be expected following basic quantum mechanics but would not be achieved in the well-known double-exchange picture [48], for in that classical approach the hole would not be able to hop at all in the $S = 1$ antiferromagnet.

ACKNOWLEDGMENTS

We are very grateful to D. Sutter and J. Chang for sharing the experimental data that was presented in Ref. [30] and which allowed us to plot Fig. 1(a). We thank E. Paris for insightful discussions. A.K. thanks the IFW Dresden for the kind hospitality. A.K. and K.W. acknowledge support by Narodowe Centrum Nauki (NCN, Poland) under Projects No. 2016/22/E/ST3/00560 and No. 2016/23/B/ST3/00839. J.v.d.B. acknowledges financial support from the German Research Foundation (Deutsche Forschungsgemeinschaft, DFG) via Grant No. SFB1143 project A5 and the support by the DFG through the Würzburg-Dresden Cluster of Excellence on Complexity and Topology in Quantum Matter-ct.qmat (EXC 2147, Project No. 39085490).

APPENDIX A: $S = 1$ t - J MODEL HAMILTONIAN EXPRESSED USING HUBBARD OPERATORS

The Hubbard operator notation [44] (for a more recent application see, for example, [45,46]) is sometimes used to

$$\begin{aligned} \mathcal{H}_t &= -t \sum_{i,\sigma} \left[\left(\sum_{o,S} X_{i+\mathbf{e}_{xz}}^{oS} \right) \left(\sum_{o',S'} X_i^{S'o'} \right) + \left(\sum_{o,S} X_{i+\mathbf{e}_{yz}}^{oS} \right) \left(\sum_{o',S'} X_i^{S'o'} \right) \right] A_{S'o'}^{o,S}, \\ \mathcal{H}_J &= J \sum_{(i,j)} \left[\left(\sum_S X_i^{SS} \right) \left(\sum_S X_j^{SS} \right) + \left(\sum_{S<1} X_i^{SS+1} \right) \left(\sum_{S>-1} X_j^{SS-1} \right) + \left(\sum_{S>-1} X_i^{SS-1} \right) \left(\sum_{S<1} X_j^{SS+1} \right) \right] \\ &\quad + \frac{1}{2} \sum_i \left\{ (\epsilon + \gamma) \left(X_i^{-11} + X_i^{1-1} \right) + (\epsilon - \gamma) \left[\left(\sum_{S<1} X_i^{SS+1} \right) \left(\sum_{S>-1} X_i^{SS-1} \right) + \left(\sum_{S<1} X_i^{SS-1} \right) \left(\sum_{S>-1} X_i^{SS+1} \right) \right] \right\}, \end{aligned}$$

where the Hubbard operators X_i^{oS} , $o = u, d, \mu, \delta$, $S = -1, 0, 1$, link the three $S = 1$ states with the four single-hole states $u = (\uparrow, xz)$, $d = (\downarrow, xz)$, $\mu = (\uparrow, yz)$, $\delta = (\downarrow, yz)$, while the Hubbard operators $X_i^{S'S}$, $S, S' = -1, 0, 1$, link different $S = 1$ states. Only 32 of the matrix elements $A_{S'o'}^{o,S}$ are nonzero (see Table I in Appendix B below for details).

APPENDIX B: DERIVATION OF THE POLARON MODEL

1. Mapping onto a polaronic model: Spin Hamiltonian (\mathcal{H}_J)

To diagonalize the spin $S = 1$ Hamiltonian discussed in the paper [cf. Eq. (1) of the main text of the paper] we start by performing two rotations of spins. First, we make a different choice of the spin quantization axis \hat{z} : In this case we pick the axis without an anisotropy term. Second, we perform a π rotation of spins around the \hat{x} axis on one of the two sublattices: such transformation maps the anticipated antiferromagnetic ground state onto a ferromagnetic state. The result is the rotated spin Hamiltonian

$$\begin{aligned} \tilde{\mathcal{H}}_J &= \sum_{(i,j)} J \left[-S_i^z S_j^z + \frac{1}{2} (S_i^+ S_j^+ + S_i^- S_j^-) \right] \\ &\quad + \gamma \sum_i (S_i^y)^2 + \epsilon \sum_i (S_i^x)^2. \end{aligned} \quad (\text{B1})$$

The next step is to utilize the Holstein-Primakoff transformation and the linear spin wave approximation using

obtain an alternative expression for the t - J model Hamiltonian. The advantage of this representation is that it is more explicit, i.e., every matrix element linking any two local (onsite) states has a different Hubbard operator associated with it.

It follows that the maximum number of Hubbard operators for a given model is the same as the square of the dimension of the local (single-site) Hilbert space (for instance, for the $S = \frac{1}{2}$ Heisenberg model, the dimension of the Hilbert space is 2 and the number of Hubbard operators is 4). In the case of the model (1), (2) the dimension of the local Hilbert space is 7, which gives 49 possible Hubbard operators. As it turns out, only 33 out of 49 operators are needed to express the Hamiltonian in terms of the Hubbard operators. The remaining 16 matrix elements are zero.

The Hamiltonian we are considering consists of two parts, $\mathcal{H} = \mathcal{H}_t + \mathcal{H}_J$. Expressed in terms of the Hubbard operators these two parts read as

the assumption that the ground state is ferromagnetic and dressed with magnons. The thus-obtained Hamiltonian is then diagonalized using the successive Fourier and Bogoliubov transformations. The resulting spin Hamiltonian reads as

$$H_J = \sum_{\mathbf{q}} \Omega_{\mathbf{q}} \beta_{\mathbf{q}}^\dagger \beta_{\mathbf{q}}, \quad (\text{B2})$$

where the magnon energies $\Omega_{\mathbf{q}}$ are given by

$$\Omega_{\mathbf{q}} = Y \sqrt{1 - \left(\frac{Z_{\mathbf{q}}}{Y} \right)^2}, \quad (\text{B3})$$

with

$$\begin{aligned} Y &= 4J + \epsilon + \gamma, \\ Z_{\mathbf{q}} &= 4J\gamma_{\mathbf{q}} + \epsilon - \gamma, \end{aligned} \quad (\text{B4})$$

with

$$\gamma_{\mathbf{q}} = \frac{1}{2} [\cos(q_x) + \cos(q_y)]. \quad (\text{B5})$$

The Bogoliubov coefficients $u_{\mathbf{q}}$ and $v_{\mathbf{q}}$ are expressed through the magnon energies $\Omega_{\mathbf{q}}$ via the standard formulas (cf. Ref. [7]).

2. Mapping onto a polaronic model: Kinetic Hamiltonian (\mathcal{H}_t)

a. Dealing with projection operators

The implicit projection operators in Eq. (2) in the main text have a relatively complex form. The easiest way to deal

with them is to construct the projected form of the two single-orbital, two-site kinetic Hamiltonians

$$(H_i^{xz})_{\mathbf{i},\mathbf{i}+\mathbf{e}_{xz}} = -t \sum_{\sigma} \tilde{c}_{\mathbf{i},xz,\sigma}^{\dagger} \tilde{c}_{\mathbf{i}+\mathbf{e}_{xz},xz,\sigma} + \text{H.c.}, \quad (\text{B6})$$

$$(H_i^{yz})_{\mathbf{i},\mathbf{i}+\mathbf{e}_{yz}} = -t \sum_{\sigma} \tilde{c}_{\mathbf{i},yz,\sigma}^{\dagger} \tilde{c}_{\mathbf{i}+\mathbf{e}_{yz},yz,\sigma} + \text{H.c.}, \quad (\text{B7})$$

step by step, that is by considering every possible hopping process and the matrix element associated with it.

We consider a single hole introduced into the half-filled ground state and H_i conserves the number of electrons in the system. Moreover, the “no double occupancy” constraint implies that there can never be three electrons on one site in the xz/yz orbitals. As a result, a single hole introduced into the system propagates leaving the number of electrons in the xz/yz orbitals on all other sites unchanged and equal to two. It follows that the only nonzero matrix elements of the two-site Hamiltonians (B6) and (B7) describe processes in which a hole hops between a doubly occupied site and a singly occupied site. Furthermore, these hoppings obey two rules:

(1) The hole can hop to the neighboring site, albeit only to an unoccupied orbital.

(2) The hole can hop to the neighboring site, albeit only if the resulting onsite wave function is not a spin singlet.

The first rule is simply the “no double occupancy” constraint and the second rule follows from the exclusion of the $S = 0$ sector of the Hilbert space discussed in the main text.

All of the above means that on each site we have either the spin triplet or one spin $S = \frac{1}{2}$ fermion on the xz/yz orbitals. This in turn implies that for each pair of neighboring sites \mathbf{i}, \mathbf{j} we can use the following basis:

$$\left\{ |\uparrow\rangle_{\mathbf{i}}, |\downarrow\rangle_{\mathbf{i}}, |\uparrow\rangle_{\mathbf{j}}, |\downarrow\rangle_{\mathbf{j}} \right\} \otimes \left\{ |\downarrow\rangle_{\mathbf{j}}, |\uparrow\rangle_{\mathbf{j}}, \frac{1}{\sqrt{2}}(|\uparrow\rangle + |\downarrow\rangle)_{\mathbf{j}} \right\}, \quad (\text{B8})$$

where the upper and lower positions are the two (xz/yz) orbitals, the arrows show spin, and the two particle states form the standard triplet. The main task now is to consider the matrix elements of (B6) and (B7) in the basis (B8).

Because the Hilbert space is 12 dimensional, there are 144 different matrix elements. However, it is easy to see that only a small number of them are nonzero. In order to find them, one can use a graphical technique illustrated in Table I.

The matrix elements listed in Table I and their complex conjugates constitute all nonzero matrix elements. In total, there are 32 of them. There are, however, some symmetries that help us write the Hamiltonian in a simpler form.

First, $(M_1, M_2, M_5, M_6, M_9, M_{10}, M_{13}, M_{14})$ and conjugates come from $(H_i^{xz})_{\mathbf{i},\mathbf{i}+\mathbf{e}_{xz}}$, the rest come from $(H_i^{yz})_{\mathbf{i},\mathbf{i}+\mathbf{e}_{yz}}$. We only need to consider one of these Hamiltonians. From now on, we will only consider $(H_i^{xz})_{\mathbf{i},\mathbf{i}+\mathbf{e}_{xz}}$.

Second, let us look at M_4 and M_{11}^* or M_{11} and M_4^* , where a star denotes complex conjugation. They represent exactly the same process but happening in the opposite direction on the lattice. M_4 and M_{11} on the other hand represent the inverse processes happening in opposite directions on the lattice. This means we need only calculate one of these matrix elements. The same is true for the pair (M_8, M_{16}) and their conjugates. This leaves us with $(M_3, M_4, M_7, M_8, M_{12}, M_{15})$.

TABLE I. Columns 1–3: a graphical technique illustrating how to find all nonzero matrix elements for the two-site Hamiltonians (B6) and (B7). We have extended the basis and split the $\frac{1}{\sqrt{2}}(|\uparrow\rangle + |\downarrow\rangle)$ state into the two “classical” states $|\uparrow\rangle$ and $|\downarrow\rangle$. After finding all nonzero matrix elements, one needs to project those back onto the triplet state. In this basis, the action of the Hamiltonian is simply to move one spin (i.e., one arrow) to the empty orbital on the right. For each initial state there is therefore only one final state. It is then enough to consider the action of the Hamiltonian on all possible initial states, as shown in the table. Each of these matrix elements has its conjugate, which represents the inverse process. Columns 4–6: the Hubbard operators associated with each of the possible processes and their respective matrix elements, as introduced in Appendix A. See there for detailed discussion.

Label	Initial state	Final state	X_i operator	X_j operator	Matrix element
M_1	$ \uparrow\rangle_{\mathbf{i}} \uparrow\rangle_{\mathbf{j}}$	$ \downarrow\rangle_{\mathbf{i}} \uparrow\rangle_{\mathbf{j}}$	X^{1u}	X^{u1}	A_{u1}^{1u}
M_2	$ \uparrow\rangle_{\mathbf{i}} \downarrow\rangle_{\mathbf{j}}$	$ \uparrow\rangle_{\mathbf{i}} \uparrow\rangle_{\mathbf{j}}$	X^{1u}	X^{d0}	A_{d0}^{1u}
M_3	$ \uparrow\rangle_{\mathbf{i}} \uparrow\rangle_{\mathbf{j}}$	$ \uparrow\rangle_{\mathbf{i}} \downarrow\rangle_{\mathbf{j}}$	$X^{1\mu}$	$X^{\mu 1}$	$A_{\mu 1}^{1\mu}$
M_4	$ \uparrow\rangle_{\mathbf{i}} \downarrow\rangle_{\mathbf{j}}$	$ \uparrow\rangle_{\mathbf{i}} \uparrow\rangle_{\mathbf{j}}$	$X^{1\mu}$	$X^{\delta 0}$	$A_{\delta 0}^{1\mu}$
M_5	$ \downarrow\rangle_{\mathbf{i}} \downarrow\rangle_{\mathbf{j}}$	$ \downarrow\rangle_{\mathbf{i}} \uparrow\rangle_{\mathbf{j}}$	X^{-1d}	X^{d-1}	A_{d-1}^{-1d}
M_6	$ \downarrow\rangle_{\mathbf{i}} \uparrow\rangle_{\mathbf{j}}$	$ \downarrow\rangle_{\mathbf{i}} \downarrow\rangle_{\mathbf{j}}$	X^{-1d}	X^{u0}	A_{u0}^{-1d}
M_7	$ \downarrow\rangle_{\mathbf{i}} \downarrow\rangle_{\mathbf{j}}$	$ \downarrow\rangle_{\mathbf{i}} \uparrow\rangle_{\mathbf{j}}$	$X^{-1\delta}$	$X^{\delta-1}$	$A_{\delta-1}^{-1\delta}$
M_8	$ \downarrow\rangle_{\mathbf{i}} \uparrow\rangle_{\mathbf{j}}$	$ \downarrow\rangle_{\mathbf{i}} \downarrow\rangle_{\mathbf{j}}$	$X^{-1\delta}$	$X^{\mu 0}$	$A_{\mu 0}^{-1\delta}$
M_9	$ \uparrow\rangle_{\mathbf{i}} \uparrow\rangle_{\mathbf{j}}$	$ \uparrow\rangle_{\mathbf{i}} \downarrow\rangle_{\mathbf{j}}$	X^{0u}	X^{u0}	A_{u0}^{0u}
M_{10}	$ \uparrow\rangle_{\mathbf{i}} \downarrow\rangle_{\mathbf{j}}$	$ \uparrow\rangle_{\mathbf{i}} \uparrow\rangle_{\mathbf{j}}$	X^{0u}	X^{d-1}	A_{d-1}^{0u}
M_{11}	$ \uparrow\rangle_{\mathbf{i}} \uparrow\rangle_{\mathbf{j}}$	$ \downarrow\rangle_{\mathbf{i}} \uparrow\rangle_{\mathbf{j}}$	$X^{0\delta}$	$X^{\mu 1}$	$A_{\mu 1}^{0\delta}$
M_{12}	$ \uparrow\rangle_{\mathbf{i}} \downarrow\rangle_{\mathbf{j}}$	$ \downarrow\rangle_{\mathbf{i}} \uparrow\rangle_{\mathbf{j}}$	$X^{0\delta}$	$X^{\delta 0}$	$A_{\delta 0}^{0\delta}$
M_{13}	$ \downarrow\rangle_{\mathbf{i}} \uparrow\rangle_{\mathbf{j}}$	$ \downarrow\rangle_{\mathbf{i}} \downarrow\rangle_{\mathbf{j}}$	X^{0d}	X^{u1}	A_{u1}^{0d}
M_{14}	$ \downarrow\rangle_{\mathbf{i}} \downarrow\rangle_{\mathbf{j}}$	$ \downarrow\rangle_{\mathbf{i}} \uparrow\rangle_{\mathbf{j}}$	X^{0d}	X^{d0}	A_{d0}^{0d}
M_{15}	$ \downarrow\rangle_{\mathbf{i}} \uparrow\rangle_{\mathbf{j}}$	$ \uparrow\rangle_{\mathbf{i}} \uparrow\rangle_{\mathbf{j}}$	$X^{0\mu}$	$X^{\mu 0}$	$A_{\mu 0}^{0\mu}$
M_{16}	$ \downarrow\rangle_{\mathbf{i}} \downarrow\rangle_{\mathbf{j}}$	$ \uparrow\rangle_{\mathbf{i}} \downarrow\rangle_{\mathbf{j}}$	$X^{0\mu}$	$X^{\delta-1}$	$A_{\delta-1}^{0\mu}$

Third, (M_3, M_7) are the same but have all spins flipped, which is a symmetry of the Hamiltonian. The same is true for (M_4, M_8) and (M_{12}, M_{15}) . Altogether, this leaves us with the classification of the nonzero matrix elements shown in Table II.

In order to obtain the second quantized form of (B6) and (B7) we need to calculate all matrix elements and construct the projected two-site Hamiltonian using

$$(H_i^{xz})_{\mathbf{i},\mathbf{i}+\mathbf{e}_{xz}} = \sum_{k,l} (H_i^{xz})_{\mathbf{i},\mathbf{i}+\mathbf{e}_{xz}}^{k,l} |k\rangle\langle l|, \quad (\text{B9})$$

TABLE II. All nonzero matrix elements of the Hamiltonians (B6) and (B7) divided into symmetry classes.

Matrix elements	Representative
$M_1, M_3, M_5, M_7 + \text{c.c.}$	M_3
$M_2, M_4, M_6, M_8, M_{10}, M_{11}, M_{13}, M_{16} + \text{c.c.}$	M_4
$M_9, M_{12}, M_{14}, M_{15} + \text{c.c.}$	M_{15}

TABLE III. The calculated values of matrix elements in each symmetry class.

Matrix elements	Rep.	Value
$M_1, M_3, M_5, M_7 + \text{c.c.}$	M_3	t
$M_2, M_4, M_6, M_8, M_{10}, M_{11}, M_{13}, M_{16} + \text{c.c.}$	M_4	$\frac{t}{\sqrt{2}}$
$M_9, M_{12}, M_{14}, M_{15} + \text{c.c.}$	M_{15}	$\frac{t}{2}$

where the vectors $|k\rangle, |l\rangle$ are written in the second quantized form. $(H_i^{xz})_{i, i+e_{xz}}^{k,l} \equiv M_j$ are the matrix elements that have been discussed above and need to be explicitly calculated (see below).

b. Calculation of the matrix elements

The matrix elements M_j can be calculated in a straightforward way. As an example, we calculate M_3 :

$$\begin{aligned} M_3 &= (\langle 0 | \tilde{c}_{i,yz,\uparrow} \tilde{c}_{j,xz,\uparrow} \tilde{c}_{j,yz,\uparrow} \rangle (-t \tilde{c}_{j,xz,\uparrow}^\dagger \tilde{c}_{i,xz,\uparrow}^\dagger) \\ &\quad \times (\tilde{c}_{j,yz,\uparrow}^\dagger \tilde{c}_{i,yz,\uparrow}^\dagger \tilde{c}_{i,xz,\uparrow}^\dagger | 0 \rangle) \\ &= t \langle 0 | 0 \rangle. \end{aligned} \quad (\text{B10})$$

M_4 and M_{15} are calculated in a similar manner. The result is shown in Table III. Once all the matrix elements are calculated, one can easily write the projected form of Eq. (2) from the main text in the second quantized form.

c. Polaronic mapping

In order to map our model onto a polaronic one, we need to introduce slave fermions (cf. Ref. [7]) using a general mapping

$$\tilde{c}_{i,\alpha,\uparrow} \rightarrow \hat{A} h_{i,\alpha}^\dagger, \quad \tilde{c}_{i,\alpha,\downarrow} \rightarrow \hat{A} h_{i,\alpha}^\dagger S_i^+, \quad (\text{B11})$$

where \hat{A} is an operator to be determined. The spinless hole operators $h_{i,\alpha}$ obey the Pauli exclusion principle and the standard anticommutation relations. The spin $S = 1$ operators obey the standard commutation relations. Finally, the spinless hole operators commute with the spin operators, which introduces an extra term in the Hamiltonian (see below). The onsite basis after this mapping is $\{|n_{xz}, n_{yz}, S_z\rangle\}$, where n_{xz} (n_{yz}) are the number of holes on the xz (yz) orbitals and S_z is the eigenvalue of the S_z operator.

d. Restricting the Hilbert space

We observe that after the polaronic mapping there are four states that do not map to any states in the old basis, namely,

$$\{|1, 0, -1\rangle, |0, 1, -1\rangle, |1, 1, 0\rangle, |1, 1, -1\rangle\}. \quad (\text{B12})$$

Evidently, these need to be projected out. One could achieve this using projection operators, but it would complicate the formula for the Hamiltonian. Another approach, presented in Ref. [7] for the $S = \frac{1}{2}$ case, is to include an extra term in the Hamiltonian with a very large energy constant $\zeta > 0$, in the spirit of the Lagrange multipliers. In our case, this term takes

the form

$$\begin{aligned} H_\zeta &= \zeta \sum_{\mathbf{i}} [(h_{i,xz}^\dagger h_{i,xz} h_{i,yz}^\dagger h_{i,yz} (S_i^z - 1)^2) \\ &\quad + (h_{i,xz}^\dagger h_{i,xz} + h_{i,yz}^\dagger h_{i,yz}) S_i^z (S_i^z - 1)]. \end{aligned} \quad (\text{B13})$$

Following the authors of Ref. [7] we will neglect this part of the Hamiltonian. It is clear that this is not without consequence. For simpler models it was shown [13] that including such constraints in the diagrammatic expansion of the Dyson equation leads to quantitative differences. We believe that the same situation happens for the $S = 1$ case studied here.

e. Linear spin wave (LSW) approximation

To arrive at the formula (5) in the main text we need to find the expressions for the operators $|k\rangle\langle l|$ appearing in Eq. (B9). We look for them in the LSW approximation. After introducing magnons via the Holstein-Primakoff transformation, the spin quantum number S_z maps onto the number of magnons quantum number n_{mag} :

$$S_z = 1, 0, -1 \rightarrow n_{\text{mag}} = 0, 1, 2, \quad (\text{B14})$$

respectively, while the fermionic quantum numbers $\{n_{xz}, n_{yz}\}$ remain the same.

In this basis, let us examine the projection operator (P_3) associated with the matrix element M_3 that was discussed above (the other cases are analogous, see below). After the sublattice rotation we obtain

$$\begin{aligned} P_3 &= |\uparrow_i \downarrow_j \downarrow_j \uparrow_i\rangle \langle \uparrow_i \downarrow_j \downarrow_j \uparrow_i| \\ &= \sqrt{2} |1, 0, 0\rangle_i |0, 0, 2\rangle_j \langle 1, 0, 1|_j \langle 0, 0, 0|_i \\ &= \sqrt{2} (h_{j,yz} h_{j,xz} h_{i,yz} a_j^\dagger a_j^\dagger |1, 1, 0\rangle_i |1, 1, 0\rangle_j) \\ &\quad \otimes (\langle 1, 1, 0|_i \langle 1, 1, 0|_j a_j^\dagger h_{j,yz}^\dagger h_{i,xz}^\dagger h_{i,yz}^\dagger). \end{aligned} \quad (\text{B15})$$

First, we notice that the projection onto the double-vacuum state, which represents two empty sites, is obsolete. Indeed, if a state survives the action of the spinless fermion creation operators on the right it survives it as one of two states:

(1) A state with four spinless holes, two on each site, in which case the projection is obsolete as this is a unique property of the vacuum.

(2) A state with three spinless holes, two on the i th site and one on the $(i + 1)$ st site. In this case the annihilation operators on the left annihilate it because two of them act on the $(i + 1)$ st site.

It is easy to see that the same is true for any of the 16 operators multiplying the matrix elements in Table I and their Hermitian conjugates.

Using this we can write P_3 as

$$\begin{aligned} P_3 &= \sqrt{2} h_{j,yz} h_{j,xz} h_{i,yz} h_{j,yz}^\dagger h_{i,xz}^\dagger h_{i,yz}^\dagger a_j^\dagger a_j^\dagger a_j \\ &\approx \sqrt{2} h_{i,xz}^\dagger h_{j,xz} a_j^\dagger a_j^\dagger, \end{aligned} \quad (\text{B16})$$

where we have neglected the normal-ordered terms with three or more spinless hole operators which go beyond our diagrammatic expansion (see Appendix B 4).

We see that P_3 is of order three in the bosonic operators. Performing similar calculations for the other 15 operators one can show that they can be divided into three groups:

- (1) of order one in bosonic operators,
- (2) of order three in bosonic operators,
- (3) of order five in bosonic operators.

In the LSW approximation we only consider the first group of terms. Consequently, only 4 amongst the 16 operators are non-negligible. These are $\{P_2, P_4, P_{10}, P_{16}\}$. Together with their respective matrix elements the four operators and their Hermitian conjugates give the projected kinetic Hamiltonian in the LSW approximation [see last two lines of Eq. (6) in the main text].

3. Mapping onto a polaronic model: Spectral functions

As discussed in the main text of the paper we are interested in calculating the following spectra function:

$$\begin{aligned} A_\alpha(\mathbf{k}, \omega) &= -\frac{1}{\pi} \text{Im}\{G_\alpha(\mathbf{k}, \omega)\} \\ &= -\frac{1}{\pi} \text{Im}\langle 0 | \tilde{c}_{\mathbf{k},\alpha,\sigma}^\dagger \frac{1}{\omega - \mathcal{H} + E_0 + i\delta} \tilde{c}_{\mathbf{k},\alpha,\sigma} | 0 \rangle, \end{aligned} \quad (\text{B17})$$

where $\tilde{c}_{\mathbf{k},\alpha,\sigma} = c_{\mathbf{k},\alpha,\sigma}(1 - c_{\mathbf{k},\alpha,\bar{\sigma}}^\dagger c_{\mathbf{k},\alpha,\bar{\sigma}})$ are the restricted hole annihilation operators. It is therefore not a one-particle Green's function.

The relation between the above-defined hole spectral function and the spinless hole spectral function is nontrivial (cf. Appendix of Ref. [7]). The latter one, that is natural to the polaronic language, is calculated from the single-particle spinless hole Green's function and reads as

$$\begin{aligned} A_\alpha(\mathbf{k}, \omega) &= -\frac{1}{\pi} \text{Im}\{G_\alpha(\mathbf{k}, \omega)\} \\ &= -\frac{1}{\pi} \text{Im}\langle 0 | h_{\mathbf{k},\alpha} \frac{1}{\omega - H + E_0 + i\delta} h_{\mathbf{k},\alpha}^\dagger | 0 \rangle. \end{aligned} \quad (\text{B18})$$

Fortunately, it was shown that for the $S = \frac{1}{2} t-J$ model the spinless hole spectral function and the hole spectral function almost coincide [11]. We assume that the same also holds also for the $S = 1 t-J$ model investigated here.

4. Self-consistent Born approximation to the Dyson equation

To obtain the Green's function $G_\alpha(\mathbf{k}, \omega)$ of Eq. (B18), and thus calculate the spectral function $A_\alpha(\mathbf{k}, \omega)$, we use the Dyson equation

$$G_\alpha(\mathbf{k}, \omega) = G_\alpha^0(\mathbf{k}, \omega) + G_\alpha^0(\mathbf{k}, \omega) \Sigma_\alpha(\mathbf{k}, \omega) G_\alpha(\mathbf{k}, \omega), \quad (\text{B19})$$

where α is an orbital index. The self-energy $\Sigma_\alpha(\mathbf{k}, \omega)$ is defined as the sum of all nonreducible diagrams starting and ending with the same vertex with an external line representing a spinless hole with momentum \mathbf{k} and orbital index α .

We calculate the self-energy $\Sigma_\alpha(\mathbf{k}, \omega)$ approximately, using the self-consistent Born approximation (SCBA):

$$\begin{aligned} \Sigma_\alpha(\mathbf{k}, \omega) &\approx \int_{-\infty}^{\infty} d\omega' \sum_{\mathbf{q}} D^0(\omega') G_\alpha(\mathbf{k} - \mathbf{q}, \omega - \omega') V_\alpha(\mathbf{k}, \mathbf{q}) \\ &\quad \times V_\alpha(\mathbf{k}, \mathbf{q})^*, \end{aligned} \quad (\text{B20})$$

where the vertex is defined as

$$V_\alpha(\mathbf{k}, \mathbf{q}) = \frac{\sqrt{2} t}{\sqrt{N}} (\gamma_{\mathbf{k}\cdot\mathbf{e}_\alpha} v_{\mathbf{q}} + \gamma_{(\mathbf{k}-\mathbf{q})\cdot\mathbf{e}_\alpha} u_{\mathbf{q}}), \quad (\text{B21})$$

and the magnon Green's function is

$$D^0(\omega) = \delta(\omega - \Omega_{\mathbf{q}}). \quad (\text{B22})$$

Using Eqs. (B21) and (B22) we obtain the self-consistent equation for the self-energy (B20) in the SCBA approximation

$$\begin{aligned} \Sigma_\alpha(\mathbf{k}, \omega) &= \sum_{\mathbf{q}} G_\alpha(\mathbf{k} - \mathbf{q}, \omega - \Omega_{\mathbf{q}}) V_\alpha(\mathbf{k}, \mathbf{q}) V_\alpha(\mathbf{k}, \mathbf{q})^* \\ &= \sum_{\mathbf{q}} \frac{V_\alpha(\mathbf{k}, \mathbf{q}) V_\alpha(\mathbf{k}, \mathbf{q})^*}{\omega + J - \Omega_{\mathbf{q}} - \Sigma_\alpha(\mathbf{k} - \mathbf{q}, \omega - \Omega_{\mathbf{q}})}. \end{aligned} \quad (\text{B23})$$

Finally, the above equation is solved numerically for the self-energy $\Sigma_\alpha(\mathbf{k}, \omega)$ on a finite mesh of \mathbf{k} and ω points (see main text of the paper).

-
- [1] E. Dagotto, *Rev. Mod. Phys.* **66**, 763 (1994).
[2] M. Imada, A. Fujimori, and Y. Tokura, *Rev. Mod. Phys.* **70**, 1039 (1998).
[3] P. A. Lee, N. Nagaosa, and X.-G. Wen, *Rev. Mod. Phys.* **78**, 17 (2006).
[4] D. I. Khomskii, *Basic Aspects of the Quantum Theory of Solids: Order and Elementary Excitations* (Cambridge University Press, Cambridge, 2010).
[5] D. I. Khomskii, *Transition Metal Compounds* (Cambridge University Press, Cambridge, 2014).
[6] S. Schmitt-Rink, C. M. Varma, and A. E. Ruckenstein, *Phys. Rev. Lett.* **60**, 2793 (1988).
[7] G. Martinez and P. Horsch, *Phys. Rev. B* **44**, 317 (1991).
[8] A. Ramšak and P. Horsch, *Phys. Rev. B* **57**, 4308 (1998).
[9] J. van den Brink and O. P. Sushkov, *Phys. Rev. B* **57**, 3518 (1998).
[10] E. Manousakis, *Phys. Rev. B* **75**, 035106 (2007).
[11] Y. Wang, K. Wohlfeld, B. Moritz, C. J. Jia, M. van Veenendaal, K. Wu, C. C. Chen, and T. P. Devereaux, *Phys. Rev. B* **92**, 075119 (2015).
[12] F. Grusdt, M. Kánasz-Nagy, A. Bohrdt, C. S. Chiu, G. Ji, M. Greiner, D. Greif, and E. Demler, *Phys. Rev. X* **8**, 011046 (2018).
[13] K. Bieniasz, P. Wrzosek, A. M. Oles, and K. Wohlfeld, *SciPost Phys.* **7**, 66 (2019).
[14] B. O. Wells, Z. X. Shen, A. Matsuura, D. M. King, M. A. Kastner, M. Greven, and R. J. Birgeneau, *Phys. Rev. Lett.* **74**, 964 (1995).
[15] S. LaRosa, I. Vobornik, F. Zwick, H. Berger, M. Grioni, G. Margaritondo, R. J. Kelley, M. Onellion, and A. Chubukov, *Phys. Rev. B* **56**, R525 (1997).
[16] C. Kim, P. J. White, Z.-X. Shen, T. Tohyama, Y. Shibata, S. Maekawa, B. O. Wells, Y. J. Kim, R. J. Birgeneau, and M. A. Kastner, *Phys. Rev. Lett.* **80**, 4245 (1998).

- [17] A. Damascelli, Z. Hussain, and Z. X. Shen, *Rev. Mod. Phys.* **75**, 473 (2003).
- [18] K. M. Shen, F. Ronning, W. Meevasana, D. H. Lu, N. J. C. Ingle, F. Baumberger, W. S. Lee, L. L. Miller, Y. Kohsaka, M. Azuma, M. Takano, H. Takagi, and Z.-X. Shen, *Phys. Rev. B* **75**, 075115 (2007).
- [19] F. C. Zhang and T. M. Rice, *Phys. Rev. B* **37**, 3759 (1988).
- [20] C. S. Alexander, G. Cao, V. Dobrosavljevic, S. McCall, J. E. Crow, E. Lochner, and R. P. Guertin, *Phys. Rev. B* **60**, R8422(R) (1999).
- [21] S. Nakatsuji and Y. Maeno, *Phys. Rev. Lett.* **84**, 2666 (2000).
- [22] T. Mizokawa, L. H. Tjeng, G. A. Sawatzky, G. Ghiringhelli, O. Tjernberg, N. B. Brookes, H. Fukazawa, S. Nakatsuji, and Y. Maeno, *Phys. Rev. Lett.* **87**, 077202 (2001).
- [23] J. S. Lee, Y. S. Lee, T. W. Noh, S.-J. Oh, J. Yu, S. Nakatsuji, H. Fukazawa, and Y. Maeno, *Phys. Rev. Lett.* **89**, 257402 (2002).
- [24] M. Cuoco, F. Forte, and C. Noce, *Phys. Rev. B* **73**, 094428 (2006).
- [25] E. Gorelov, M. Karolak, T. O. Wehling, F. Lechermann, A. I. Lichtenstein, and E. Pavarini, *Phys. Rev. Lett.* **104**, 226401 (2010).
- [26] S. Kunkemöller, D. Khomskii, P. Steffens, A. Piovano, A. A. Nugroho, and M. Braden, *Phys. Rev. Lett.* **115**, 247201 (2015).
- [27] C. G. Fatuzzo, M. Dantz, S. Fatale, P. Olalde-Velasco, N. E. Shaik, B. Dalla Piazza, S. Toth, J. Pellicciari, R. Fittipaldi, A. Vecchione, N. Kikugawa, J. S. Brooks, H. M. Rønnow, M. Gioni, C. Rüegg, T. Schmitt, and J. Chang, *Phys. Rev. B* **91**, 155104 (2015).
- [28] S. Kunkemöller, E. Komleva, S. V. Streltsov, S. Hoffmann, D. I. Khomskii, P. Steffens, Y. Sidis, K. Schmalzl, and M. Braden, *Phys. Rev. B* **95**, 214408 (2017).
- [29] A. Jain, M. Krautloher, J. Porras, G. H. Ryu, D. P. Chen, D. L. Abernathy, J. T. Park, A. Ivanov, J. Chaloupka, G. Khaliullin *et al.*, *Nat. Phys.* **13**, 633 (2017).
- [30] D. Sutter, C. G. Fatuzzo, S. Moser, M. Kim, R. Fittipaldi, A. Vecchione, V. Granata, Y. Sassa, F. Cossalter, G. Gatti *et al.*, *Nat. Commun.* **8**, 15176 (2017).
- [31] G. Zhang and E. Pavarini, *Phys. Rev. B* **95**, 075145 (2017).
- [32] L. Das, F. Forte, R. Fittipaldi, C. G. Fatuzzo, V. Granata, O. Ivashko, M. Horio, F. Schindler, M. Dantz, Y. Tseng, D. E. McNally, H. M. Rønnow, W. Wan, N. B. Christensen, J. Pellicciari, P. Olalde-Velasco, N. Kikugawa, T. Neupert *et al.*, *Phys. Rev. X* **8**, 011048 (2018).
- [33] S. Riccò, M. Kim, A. Tamai, S. McKeown Walker, F. Y. Bruno, I. Cucchi, E. Cappelli, C. Besnard, T. K. Kim, P. Dudin, M. Hoesch, M. J. Gutmann, A. Georges, R. S. Perry, and F. Baumberger, *Nat. Commun.* **9**, 4535 (2018).
- [34] D. G. Porter, V. Granata, F. Forte, S. Di Matteo, M. Cuoco, R. Fittipaldi, A. Vecchione, and A. Bombardi, *Phys. Rev. B* **98**, 125142 (2018).
- [35] D. Pincini, L. S. I. Veiga, C. D. Dashwood, F. Forte, M. Cuoco, R. S. Perry, P. Bencok, A. T. Boothroyd, and D. F. McMorrow, *Phys. Rev. B* **99**, 075125 (2019).
- [36] H. Gretarsson, H. Suzuki, H. Kim, K. Ueda, M. Krautloher, B. J. Kim, H. Yavaş, G. Khaliullin, and B. Keimer, *Phys. Rev. B* **100**, 045123 (2019).
- [37] Y. Maeno, H. Hashimoto, K. Yoshida, S. Nishizaki, T. Fujita, J. G. Bednorz, and F. Lichtenberg, *Nature (London)* **372**, 532 (1994).
- [38] G. Khaliullin, *Phys. Rev. Lett.* **111**, 197201 (2013).
- [39] A. Akbari and G. Khaliullin, *Phys. Rev. B* **90**, 035137 (2014).
- [40] T. Feldmaier, P. Strobel, M. Schmid, P. Hansmann, and M. Daghofer, [arXiv:1910.13977](https://arxiv.org/abs/1910.13977).
- [41] J. C. Slater and G. F. Koster, *Phys. Rev.* **94**, 1498 (1954).
- [42] A. B. Harris, A. Aharony, O. Entin-Wohlman, I. Y. Korenblit, and T. Yildirim, *Phys. Rev. B* **69**, 094409 (2004).
- [43] K. Chao, J. Spalek, and A. Oles, *J. Phys. C: Solid State Phys.* **10**, L271 (1977).
- [44] J. Hubbard, *Proc. R. Soc. London A* **277**, 237 (1964).
- [45] P. Coleman, C. Pépin, and J. Hopkinson, *Phys. Rev. B* **63**, 140411(R) (2001).
- [46] N. M. Plakida, *Condens. Matter Phys.* **5**, 707 (2002).
- [47] S. Nakatsuji, S.-i. Ikeda, and Y. Maeno, *J. Phys. Soc. Jpn.* **66**, 1868 (1997).
- [48] C. Zener, *Phys. Rev.* **82**, 403 (1951).
- [49] G. F. Reiter, *Phys. Rev. B* **49**, 1536 (1994).